Smart Materials and Structures

Shape memory alloy tube actuators inherently enable internal fluidic cooling for a robotic finger under force control

To cite this article before publication: Craig Ades *et al* 2020 *Smart Mater. Struct.* in press https://doi.org/10.1088/1361-665X/ab931f

Shape Memory Alloy Tube Actuators Inherently Enable Internal Fluidic Cooling for a Robotic Finger Under Force Control

Craig J. Ades, Savas Dilibal, and Erik D. Engeberg

Florida Atlantic University, Boca Raton, Florida
Gedik University, Istanbul, Turkey

***Abstract*—This paper presents the design, control and evaluation of a novel robotic finger actuated by shape memory alloy (SMA) tubes which intrinsically afford an internal conduit for fluidic cooling. The SMA tubes are thermomechanically programmed to flex the robotic finger when Joule heated. A superelastic SMA plate provides a spring return motion to extend the finger when cooling liquid is pumped through the internal channel of the SMA tube actuators. The mechanical design and nonlinear force controller are presented for this unique robotic finger. Sinusoidal and step response experiments demonstrate excellent error minimization when operated below the bandwidth which was empirically determined to be 6 rad/s. Disturbance rejection experiments are also performed to demonstrate the potential to minimize externally applied forces. This method of internal liquid cooling of Joule heated SMA tubes simultaneously increases the system bandwidth and expands the potential uses of SMA actuators for robotic applications. The results show that this novel robotic finger is capable of precise force control and has a high strength to weight ratio. The finger can apply a force of 4.35 N and has a mass of 30 g. Implementing this design into wearable prosthetic devices could enable lightweight, high strength applications previously not achievable.**

***Index Terms*—distributed parameter systems, nonlinear control, robotic finger, shape memory alloy**

1. INTRODUCTION

The shape memory effect (SME) and superelasticity are two advantageous properties of SMAs. With the SME, SMA actuators can be thermomechanically programmed to change shape when heated above their phase transition temperatures. The superelastic (SE) property enables SMAs to completely recover from large deformations [1–3]. Combined together, the SME and SE properties are very desirable for many robotic applications [4–6]. SMAs can be manufactured in many different form factors, including wires [7], springs [8, 9], plates [10], and tubes [11–13]. In order to actuate SMAs that are integrated into robotic designs, the smart materials are often Joule heated above their phase transition temperature so that they contract and actuate a joint [4, 14]. The heating portion of the actuation stroke occurs very rapidly relative to the rather slow cooling phase of SMA when the actuator attempts to return to its initial state [3]. The slow cooling phase is typically the limiting factor in the actuator bandwidth, which has been a hindrance to the widespread application of SMA to robotic mechanisms. Micro scale SMA actuators have been shown to respond in the kilohertz frequency range [3], but this speed deteriorates rapidly as they approach the size needed for larger applications such as robotic fingers and hands [15].

There have been efforts to increase the actuation bandwidth of SMA actuators by cooling them quickly. The use of forced air convection [9], heat sinks, thermally conductive grease, oil immersion, and glycol mixed with water have enabled more rapid cooling [6]. Also, SMA plates submerged in water have been demonstrated to increase the actuation bandwidth of a human-inspired robotic finger [10]. Antagonistic actuation [7] or selective heating/cooling of SMA components has also been used in the past to improve the low bandwidth drawback [14].

SMA actuators can exert large forces relative to their weight [1, 2, 5, 16]. For this reason, SMAs have been incorporated into the mechanical design of robotic fingers and manipulators [14, 16–22]. These lightweight actuators could be particularly useful in wearable robotic applications, such as prosthetic hands [5, 15, 24–26]. SMA actuators for robotic hands have typically taken the form factor of a SMA wire or spring that is used to actuate a revolute joint [17–22, 27], with few exceptions such as the biomimetically programmed SMA plates shown in [10].

This paper provides several novel contributions relative to all the prior research on SMA actuators for robotic hands that has occurred in the past [28, 29]. The first time use of SMA actuators in a tube form factor for a robotic finger is presented, where the SMA tubes are thermomechanically programmed to bend and actuate a finger-like linkage mechanism. An additional source of novelty and functionality is that the use of SMA tubes inherently provides an internal channel through which water is pumped to enable rapid cooling of the Joule heated SMA tube actuators. SE SMA plates are situated antagonistically in parallel with the

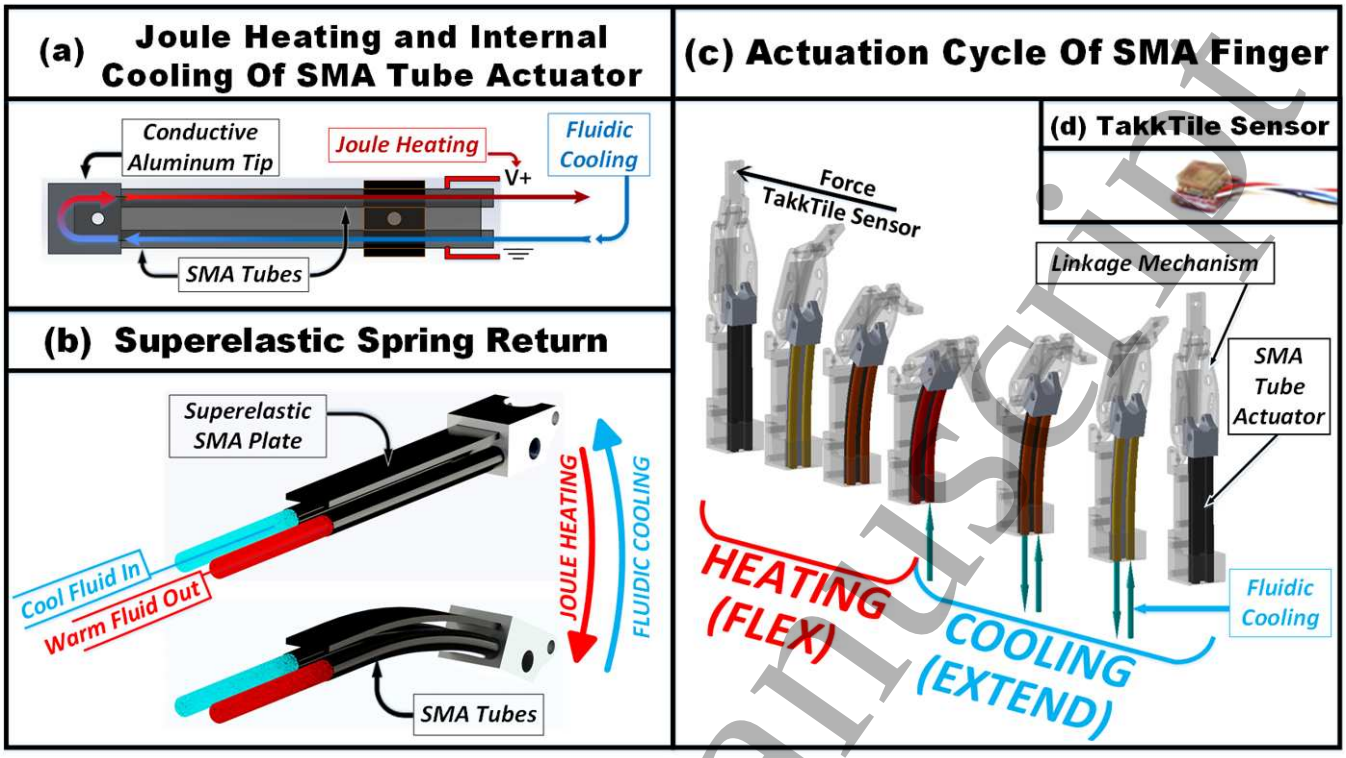

Fig. 1. Actuation concept for flexing and extending the mechanical linkage using the designed SMA actuator. (a) Electrical connection for Joule heating the SMA tube actuators and water flow through the SMA tubes enables internal cooling. (b) The SMA tubes bend when Joule heated. The antagonistically situated SE SMA plate functions as a spring return when the tubes are internally cooled with water. (c) The SMA actuation system is installed in an external finger-like linkage mechanism to amplify the range of motion. (d) The TakkTile fingertip force sensor was integrated into the tip of the finger to enable force control.

SMA tubes to provide a passive spring return motion when the tubes are internally cooled, reducing the control complexity of the robotic finger. This internal cooling concept increases the range of possible applications of SMA actuators in the field of robotics by allowing the cooling of the SMA tubes to be achieved in a non-submerged environment, opening the doors to robotic applications of SMA actuators. Collectively, these design traits produce a novel, compact, lightweight actuator with low control complexity and a high strength to weight ratio.

A preliminary design and position control of this actuation concept have been presented at a conference [30]. This journal paper provides extensive contributions over that which was previously presented through a new linkage mechanism to amplify the motion of the SMA tube actuators, integration of a TakkTile fingertip force sensor [31] into the fingertip, the design of a nonlinear force controller, and evaluation of the step and frequency responses of the system under force control. In addition to the previously mentioned novelty, this SMA actuation concept demonstrates non-obvious design features over other SMA actuation methods that have been patented [35], and has not been previously published by other researchers in scientific literature, to the best knowledge of the authors.

2. SMA Finger Actuator Design

2.1 Antagonistic Actuation Concept

The novel SMA finger is comprised of an antagonistic actuator system made from a pair of SME SMA tubes arranged in a 'U' formation (Fig. 1(a)). The tubes bend when Joule heated and SE SMA plates provide a natural spring return motion when the tubes are cooled by water being pumped through the internal cavity of the tubes (Fig. 1(a),(b)). This produces a multi-input single output (MISO) electromechanical-fluidic system (Fig. 1(a)). A finger-like linkage mechanism was fabricated to increase the actuator's range of motion (Fig. 1(c)). A TakkTile force sensor was integrated into the tip of the finger, enabling force feedback (Fig. 1(d)).

The finger is fully extended when in a cooled state (Fig. 1(c)). When the SMA tubes are Joule heated they bend due to the

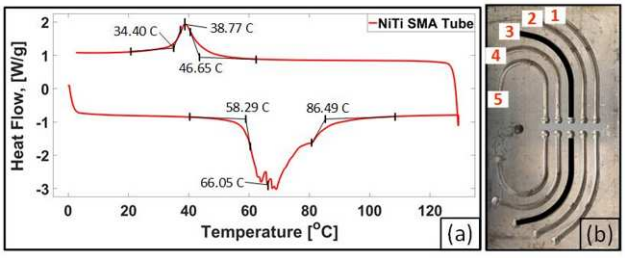

Fig. 2. (a) Differential scanning calorimetry performed to determine temperatures where the SMA tube material phase transitions occur. (b) Aluminum mold used to thermomechanically program the SMA tubes sequentially, starting at channel 1 and ending at channel 3.

thermomechanical programming process (described subsequently), and the tube actuator overcomes the opposing spring return force from the SE SMA plate. While Joule heated, the actuator continues to bend until reaching the maximum range of motion achievable (Fig. 1(b),(c)) which is the result of the chosen thermomechanical shape programming process. Pumping water through the inner cavity of the SMA tubes cools the material, resulting in the SMA tube force exerted to decrease, allowing the SE spring return to overcome the tube force, producing a return back to the initial posture (Fig. 1(b),(c)).

2.2 SMA Material Properties

The SME SMA NiTi tubes have an outer diameter of 4 mm, wall thickness of 0.35 mm, length of 76.2 mm, mass of 2.79 g and were purchased from Memry (Weil am Rhein, Germany). The tubes each have a resistance of 30 mΩ. The SE SMA NiTi plate measures 1.19 mm thick, 9.53 mm wide, 63.5 mm in length and has a mass of 8.87 g.

Differential scanning calorimetry (DSC) was performed on the NiTi SMA tubes with a TA Instruments Q10 (New Castle, DE) to determine the austenite and martensite phase transition temperatures. The austenite and martensite phase transition start and finish temperatures are shown in Fig. 2(a). Practically speaking, these temperatures indicate when the Joule heated SMA tubes will flex or extend due to the thermomechanical programming process.

2.3 Thermomechanical Programming of SMA Tube Actuators

In order to use the SMA tubes to actuate a robotic finger, they needed to be thermomechanically programmed to flex when heated above the phase transition temperature. To that end, a mold was created from an aluminum plate using a CNC machine (Fig. 2(b)). The mold was designed with five increasingly aggressive targets for thermomechanically programming the SMA tubes. Initially, a pair of tubes was placed in the first channel of the mold to constrain motion when heated in a Beuler oven set to 530˚C for 7 minutes. The mold was removed and immediately quenched in water. Next, ten cycles of material actuation cycling was performed. This was accomplished by straightening the tubes manually, applying heat to thermally flex the tubes to full flexion and repeating the process. These ten cycles were repeated for each subsequent channels in the mold, starting at channel 1 and ending at channel 3 (Fig. 2(b)). Shape programming was achieved progressively along each subsequent channel in the mold to prevent buckling since the SMA tube has a limited deformation range prior to programming. Ultimately, it was found empirically that the third channel in the mold yielded the best results whereas the fourth and fifth channel strained the SMA tubes beyond a recoverable amount.

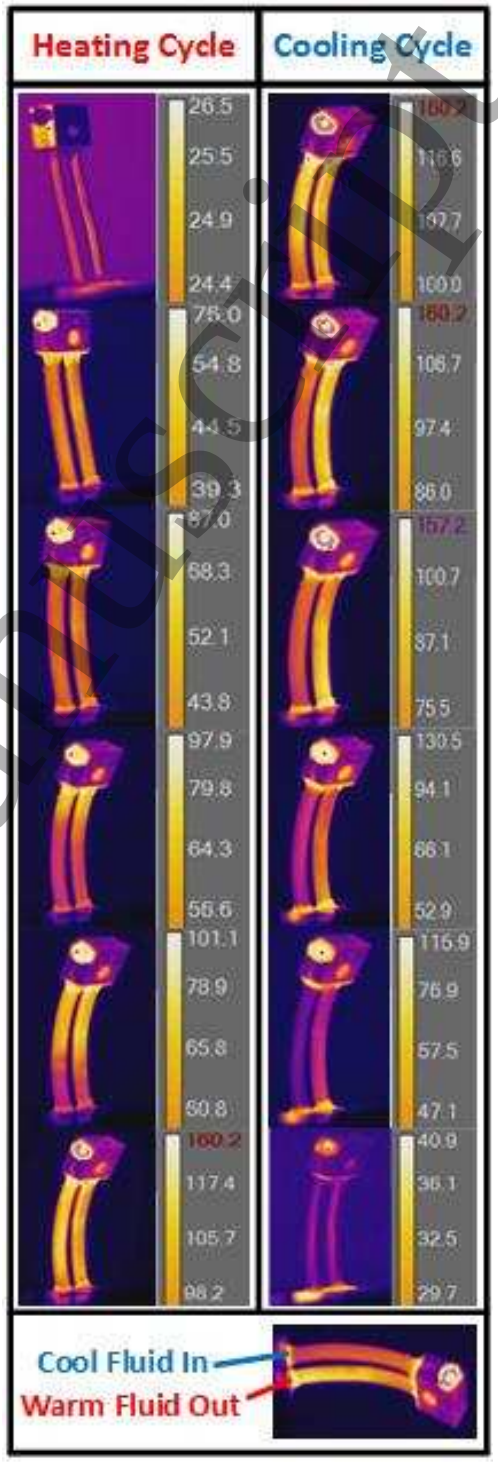

Fig. 3. Thermal imaging of the SMA tubes during Joule heating (left) and water cooling (right). Temperature units are Celsius.

2.4 SMA Tube Water Flow and Electrical Connections

After the two SMA tubes were thermomechanically programmed, they were mechanically coupled together in series with a rectangular adaptor machined out of aluminum (Fig. 1(a)). This connector allowed a continuous stream of cooling water to enter one end of a tube and exit from the far end of the second tube (Fig. 1(c)). This same series configuration of SMA tubes also provides electrical conductivity to be exploited for Joule heating of the tubes (Fig. 1(a)) via pulse width modulation (PWM). The SMA tubes were placed within rubber insulating tubes for electrical and thermal insulation.

The PWM Joule heating is facilitated by a bank of inductors to reduce the ripple current and prevent damage to the onboard capacitors. Each of the inductors used had an inductance of 100μH (Digikey, 1140-101K-RC). Eight inductors were combined together with two sets of four in parallel with the two parallel configurations combined in series to achieve a total inductance of

50μH. For the PWM boards, two Syren 50A PWM drivers were used, one for Joule heating the tubes and the other for controlling the water pump. These PWM drivers receive an analog input that is proportionally converted into a duty cycle to drive the water pump or to heat the SMA tubes.

The cooling system consists of a 12 V water pump connected to the inlet of the SMA actuator (Fig. 1(a)), powered by the PWM driver. The electrical side of the cooling system is connected to MATLAB/Simulink using a National Instruments PCIe-6323 PCI card and an SCB-68A connector block.

2.5 Thermal Imaging of SMA Tubes

Thermal imaging was performed to determine the Joule heating and fluidic cooling characteristics of the SMA tubes using a FLIR T650SC camera (FLIR, Wilsonville, Oregon), (Fig. 3). The SMA tubes are initially straight. As they are Joule heated, they flex (Fig. 3, left side). When water is pumped through the internal conduit of the tubes, they relax (Fig. 3, right side). Note that neither the rubber insulation for the SMA tubes nor the SE SMA spring return plate were used in this experiment to prevent occluding the view of the thermal camera.

2.6 Finger-Like Linkage Design

A linkage mechanism was designed to amplify the range of motion of the actuators within the framework of a two degree of freedom (DOF) model of a human finger (Fig. 1(c)) [32] that are commonly used in prosthetic hands like the i-limb [33]. The underactuated design chosen has one DOF where the motion of the distal phalanx is coupled to the proximal phalanx. The actuated DOF is where the rectangular aluminum tip of the SMA tube actuators connects to the slot in the proximal phalanx by means of a sliding pin joint. This translates into rotation of both the joints of the finger. The linkage components were cut first on a waterjet and then CNC machined on a 3-axis mill. The total mass of the system is 30 g including the linkage and tube actuators.

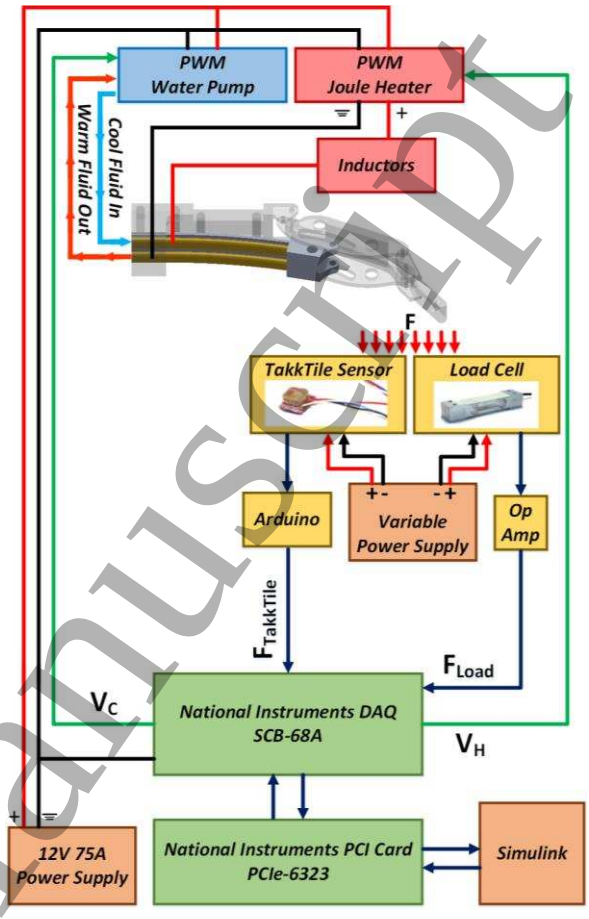

Fig. 4. System level diagram showing electrical connections to the data acquisition unit and the controller inputs/outputs.

2.7 Tactile Force Sensing

A TakkTile sensor (RIGHTHAND Robotics, MA, USA) was embedded into the distal phalanx of the linkage to measure the force, $F_{TakkTile}$, at the fingertip (Fig. 1(c),(d)). The TakkTile sensor is a barometric pressure sensor embedded onto a PCB that outputs a digital signal related to the applied force [31]. The digital TakkTile sensor signal was sampled using an Arduino Mega.

The TakkTile sensor also has a thermocouple embedded on the PCB. Thermal compensation was implemented to overcome sensitivity to ambient heat fluctuations and mitigate thermal drift. Thermal data were analyzed and a calibration curve implemented using the temperature to compensate for force drift as a result of temperature fluctuations.

A calibrated load cell (ESP-35, Transducer Techniques, Temecula, USA) was used as an external force (F_{Load}) measurement system to calibrate the TakkTile sensor. This was accomplished by heating the SMA tubes, in turn causing the linkage mechanism to flex so that the TakkTile sensor increased the force applied upon the external load cell. Forces from both sensors were simultaneously measured in Simulink to confirm that the TakkTile sensor was accurately measuring applied forces (Fig. 4).

3. METHODS

Figure 4 shows the system level architecture. A nonlinear controller was designed to provide force feedback control. This allowed the force tracking ability, the operational bandwidth, step responses and percent overshoot to be measured. Accordingly, sinusoidal trajectories and step inputs with low and high amplitudes were evaluated during force control. Tests were also conducted to demonstrate the ability to reject force disturbances.

3.1 Force Controller for SMA Actuated Robotic Finger

The nonlinear error-based force controller for this novel MISO finger is shown in Fig. 5. Force error is minimized antagonistically by utilizing Joule heating and fluidic cooling of the SME SMA tubes with PWM drivers for each subsystem. For positive error the Joule heater is activated, maintaining a small amount of fluidic cooling with a set maximum saturation limit. This causes the finger to flex and increases the applied force when in contact with the environment. Alternatively, negative force

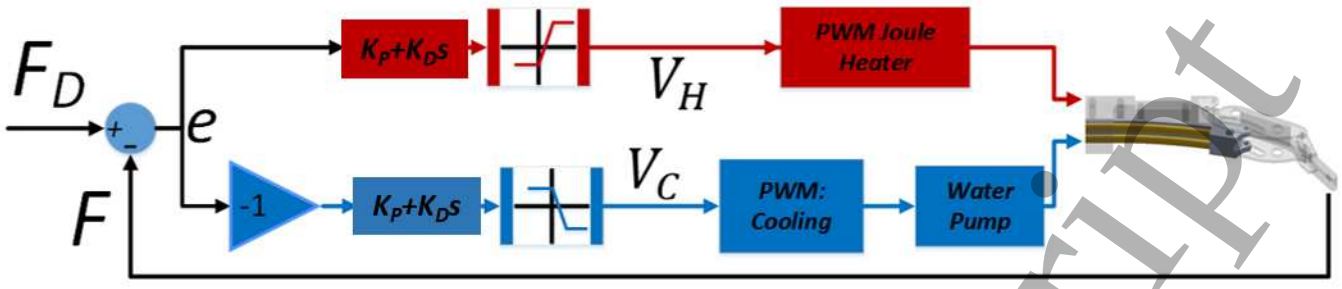

Fig. 5. Force feedback controller diagram illustrating the process for achieving force control using Simulink. The error signal is split into two parts, one to control Joule heating of the SMA tubes, and another path to pump cooling water through the internal conduit of the tubes.

error activates the fluidic cooling, maintaining a small amount of Joule heating that also has a maximum saturation limit. This causes the SE SMA plates to force a return motion, reducing the force applied by the finger as the SME SMA tubes are cooled and extended. For each of the presented modes, implementing this antagonistic mode of actuation provides increased stability when transitioning from flexing to extending and vice versa.

Due to the TakkTile sensor saturating above 0.785 N, a load cell was implemented to measure forces exceeding this saturation limit. Depending upon whether the force feedback is from the incorporated TakkTile sensor ($F_{TakkTile}$) or the external load cell, (F_{Load}), the measured fingertip force is:

$$F = \begin{cases} F_{TakkTile}, & Fingertip\ Sensor \\ F_{Load}, & External\ Sensor \end{cases} \quad (1)$$

To control the force, an error (e) was formed as the difference between the desired force, F_D, and the measured force, F:

$$e = F_D - F \quad (2)$$

Next, error manifolds were formed for both the Joule heating and water cooling subsystems:

$$S_i = K_{P,i}e + K_{D,i}\dot{e} \quad (3)$$

Here the subscript i ∈ H, C denotes the Joule heating or water cooling paths of the MISO force controller, respectively. $K_{P,i}$ and $K_{D,i}$ are the proportional and derivative gains for the heating and cooling manifolds, respectively. The saturation of these manifolds was taken to aggressively minimize the force error. Thus, the voltage control law for both the heating and cooling PWM drivers is:

$$V_i = \beta_i sat(S_i) \quad (4)$$

where

$$\beta_H = \begin{cases} \beta_H, & e \geq -\lambda_H \\ 0, & e < -\lambda_H \end{cases} \quad (5)$$

and

$$\beta_C = \begin{cases} \beta_C, & e \leq \lambda_C \\ 0, & e > \lambda_C \end{cases} \quad (6)$$

β_i represents the upper bound estimates on the torques that are acting against the robotic finger. λ_i are positive constants that set the threshold cutoff values to control the overlap of the heating and cooling actions. This controller was implemented in MATLAB/Simulink using the Realtime Windows target kernel and a sample rate of 1 KHz.

V_i are the voltages that are the analog inputs that are directly related to the duty cycle of each of the Syren PWM drivers, which have a 0-5V analog voltage input with a 10 bit resolution. These Syren motor drivers internally convert the analog input voltages, V_i, into a PWM waveform with a typical H-bridge architecture. Thus, the amplitude of the two voltages input to the two Syren PWM drivers is a direct correlation to duty cycle.

This control system has a variable structure control. In many ways it resembles a sliding mode control law with a partially linearized switching function that is based on the error manifold. However, since this is a MISO system, we split the error state into two parallel paths that were passed into the controllers for the SMA Joule heater and cooling pump. Partially linearizing the control laws was necessary to prevent system chatter and perpetual oscillations; nevertheless, the error states of the MISO system were minimized in finite time with each operational condition, consistent with well-accepted nonlinear control theory [36].

3.2 Force Controller Parameters

The bounds of operation, β_i, were chosen to provide maximum robustness against externally applied disturbances and to minimize the time required to drive the force error to zero. Practically speaking, this necessitated setting the β_i, values to the maximum permissible levels for the cooling pump and SMA Joule heating PWM drivers. The slopes of the error manifolds for each controller were determined by choice of the K_P and K_D terms which dictated the speed with which the error state was minimized. We empirically determined these values to provide a solid tradeoff between speed of system response and propensity for oscillations and chatter. From equations (5) - (6), the λ_i values specified the error overlap between the heating and cooling control laws. These values of λ_i were initially determined based on the SMA material properties regarding the material phase transition temperatures to and from austenite/martensite that were determined via differential scanning calorimetry in Fig. 2(a). The overlap in the heating/cooling thresholds (λ_i values) nominally maintained the fluid internal to the SMA tubes at a temperature very near the SMA phase transition temperature so that the system bandwidth could be increased. When the force error was greater than the heating threshold (λ_H), the system responded faster because the water within the SMA tubes was near the SMA phase transition temperature, which was considerably higher than room temperature (Fig. 2(a)). These λ_i thresholds were initially determined by SMA material phase transition temperatures (Fig. 2(a)), but were refined during initial experiments based on empirical observations.

3.3 Range of Motion and Maximum Force Experiments

To ascertain the range of motion (ROM), the robotic finger began in the fully cooled state (Fig. 6(a)). The finger was actuated while not in contact with the environment until increased heat no longer caused motion. The range of motion of the distal phalanx was calculated as the final angle minus the initial angle. This angle was calculated via images input into Kinovea [53] to track the finger actuation motion (Fig. 6). In addition to this, the angles were measured on the computer screen using a physical protractor held to the screen; the two measurements agreed.

To determine the maximum force the robotic finger can apply, it was positioned over the external load cell and the finger was actuated until the measured force on the load cell no longer increased with additional heating. The water pump was then driven to internally cool the tubes and reduce the applied force. During the max force experiment, the posture of the finger was approximately the same as in Fig. 6(b). Both the TakkTile sensor and the load cell were used to measure the maximum force and confirm calibration.

3.4 Sinusoidal Force Tracking and Frequency Response

Sinusoidal force tracking was performed for frequencies ranging from 1 rad/s to 10 rad/s with 20 cycles recorded per frequency. The desired force (input) sine wave had a bias of 0.491 N and an amplitude of 0.2943 N. The 20 cycles were gathered after allowing the system to achieve steady state. This data was used to quantify the absolute mean force tracking error for each of the aforementioned frequencies.

The same sinusoidal tracking dataset was used to determine the operational bandwidth of the finger and the frequency response of this novel SMA tube actuated finger. To that end, the amplitude ratio of the measured force and the desired force (F_D) was calculated in dB for each frequency. Similarly, the phase lag between F_D and F were also obtained experimentally from the sine wave tracking experiments.

3.5 Step Response: Force Tracking

The finger was subjected to step inputs with amplitudes of 0.245 N (half amplitude) and 0.491 N (high amplitude) at frequencies ranging from 1 to 10 rad/s to test the system for the ability to precisely control the applied force, $F_{TakkTile}$. As in previous tests, this was executed for 20 repetitions per frequency to ensure the results are repeatable and consistent. The absolute mean tracking error and percent overshoot were calculated for each frequency.

3.6 Disturbance Rejection

To demonstrate the ability of the nonlinear force controller to reject force disturbances, the SMA finger was tasked to track a sine wave input while the operator applied an external disturbance to the load cell to oppose motion in both the heating and cooling phases. This was performed separately to demonstrate the effectiveness of the MISO controller in both heating and cooling phases of control. The load cell was used as the feedback signal in these experiments to allow measurements of forces beyond the limit of the TakkTile sensor.

4. RESULTS

4.1 Range of Motion and Maximum Force

The total angular rotation of the distal phalanx with respect to the joint of actuation of this novel robotic finger from fully cooled (Fig. 6(a)) to fully heated (Fig. 6(d)) is 63° (Fig. 6). This angular rotation was calculated as the sum of angular changes of the proximal and distal links: (45° – 15°) + (53° – 20°) = 63°. This is comparable to the range of motion of the distal phalanx of human fingertips [27].

The maximum force the finger can apply is 4.346 N (Fig. 7), which is comparable to commercially available prosthetic hands such as the Vincent and bebionic hands [33, 34]. The force measured by the Takktile sensor saturated at 0.785 N (Fig. 7). The calibrated TakkTile force sensor signal shows a close correlation to the external load cell prior to saturation.

4.2 Sinusoidal Force Tracking and Frequency Response

For comparison purposes, illustrative sinusoidal force tracking data is shown for frequencies of 1 rad/s (Fig. 8(a)-(d)) and 7 rad/s (Fig. 8(e)-(f)). The robotic finger could precisely track sinusoidal inputs with minimal tracking error on the lower frequency range of the spectrum (Fig. 8(a),(b)). The cooling and heating saturation functions (4) caused the control voltages for the low frequency to rapidly switch (Fig. 8(c),(d)), keeping the force error very near 0 N (Fig. 8(b)). In contrast, force tracking error was larger for higher frequencies (Fig. 8(f)) because of the force attenuation (Fig. 8(e)). Voltage control laws (V_i) switched between maximum and minimum permissible values with much lower frequency in this case to drive the actuator at the maximum possible speed (Fig. 8(g),(h)).

The heating portion of the experiments consistently demonstrated a quicker response compared to the cooling portion. The difference in response rates during the heating and cooling portions of the actuator operation can be understood based on the different principles of heat transfer during these two different modes. This is further explained in the discussion section of this paper. The absolute mean and standard deviation of the tracking error for sine wave tracking was excellent for low frequencies of operation, and then generally increased with actuation frequency (Fig. 9, Fig. 10(a)-(d)), which is typical of most electromechanical devices.

The sinusoidal force tracking data from these experiments were used to generate the frequency response and to determine the operational bandwidth of the system (Fig. 10(e),(f)). A 3 dB drop was observed at 6 rad/s. Thus, the system bandwidth is

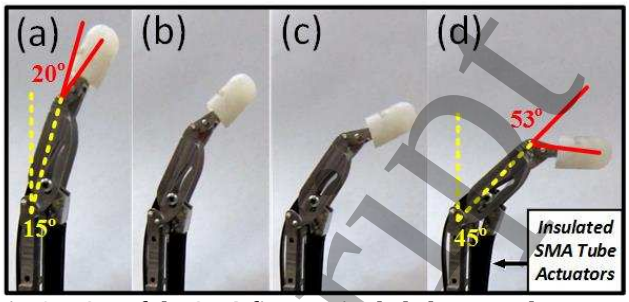

Fig. 6. ROM of the SMA finger. Distal phalanx angular change is red, proximal phalanx angular change is yellow. The location of the insulated tube actuators is labeled in (d).

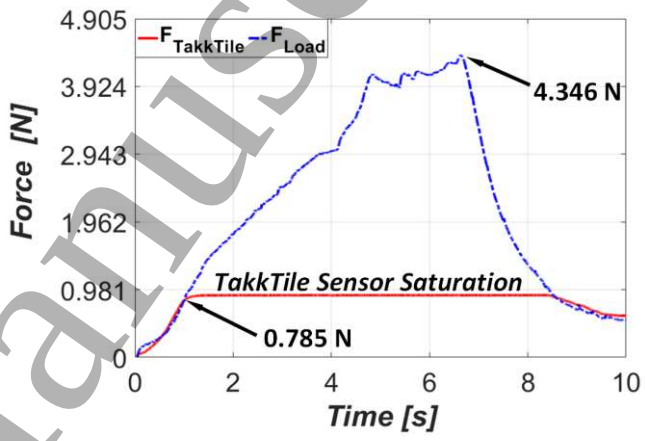

Fig. 7. Maximum force using the load cell and the embedded TakkTile sensor. The TakkTile sensor saturated at 0.785 N and the load cell measured the true max force at 4.346 N.

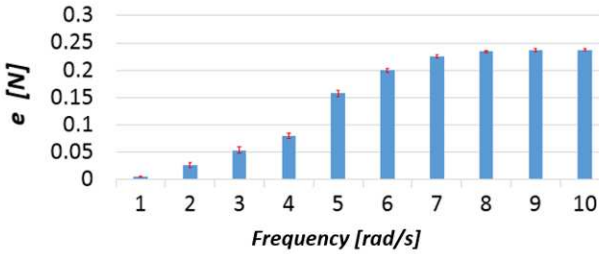

Fig. 9. Mean and standard deviation of the force tracking error for sinusoidal inputs with frequencies from 1-10 rad/s.

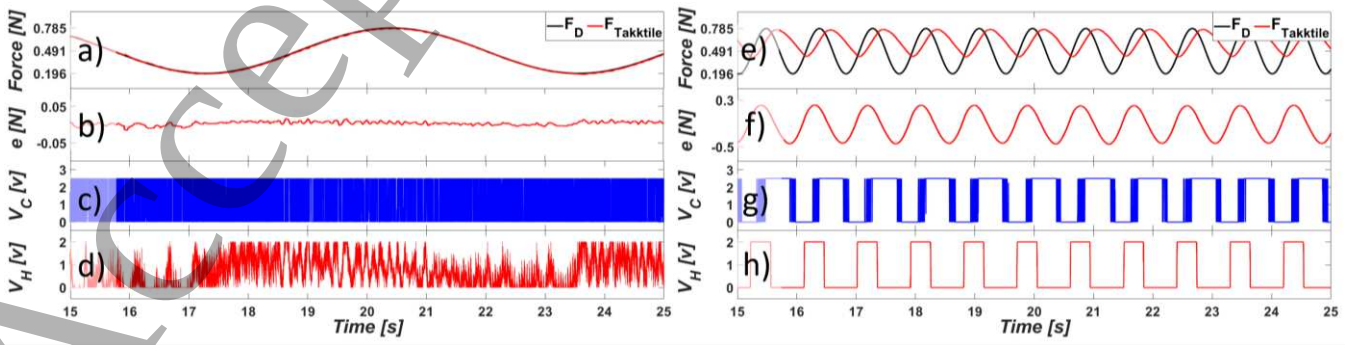

Fig. 8. (a) 1 rad/s force tracking, (b) error, (c) cooling and (d) heating control voltages during cyclic actuation were applied. (e) 7 rad/s force tracking, (f) error, (g) cooling and (h) heating control voltages during cyclic actuation were applied.

approximately 6 rad/s where a 70° phase lag was also observed. As expected, the amplitude ratio (F/F_D) decreased (Fig. 10(e)) while the phase lag increased (Fig. 10(f)) as the frequency of the input increased.

4.3 Step Response: Force Tracking

Illustrative step response data from high and half amplitude steps demonstrate excellent control of steady state force with minimal overshoot (Fig. 11). The correlation between the force error and the saturations of the heating and cooling manifolds (4) is demonstrated in Fig. 12 for a 4 rad/s step response cycle. High frequency switching between the maximum and minimum levels of the saturation threshold for the cooling and heating manifolds occurred due to the aggressive gains chosen to rapidly minimize force error. The mean and standard deviation of the tracking errors from the step response experiments showed a general increase with frequency until plateauing near a frequency of 8 rad/s (Fig. 13).

The mean and standard deviation of the percent overshoot from these step inputs was reasonably low, generally less than 5% (Fig. 14). Note that there was no overshoot with frequencies that had the half amplitude above 6 rad/s and there was no overshoot on high amplitude step responses above frequencies of 4 rad/s. This is largely because there was insufficient time to reach the desired force while tracking the high frequency square waves as exemplified with the 7 rad/s frequency (Fig. 11(c)).

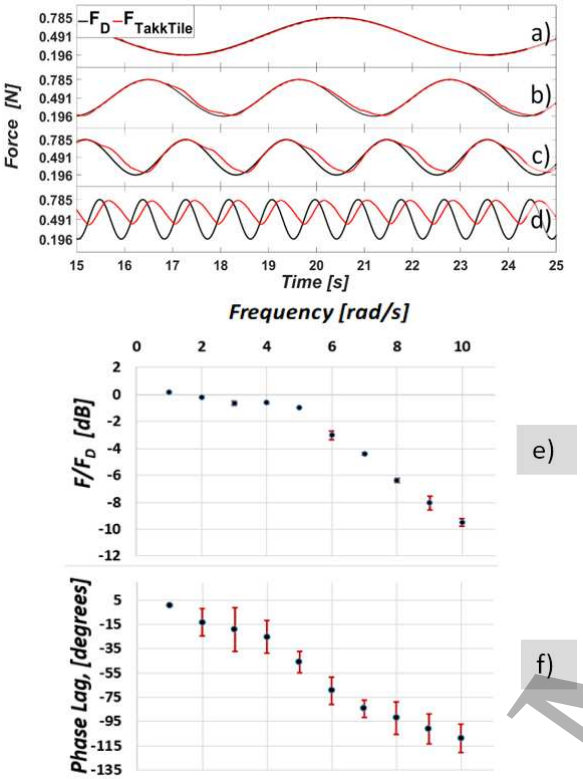

Fig. 10. Sinusoidal force tracking results to demonstrate force control capabilities and the frequency response during cyclic actuation. The frequencies shown are (a) 1 rad/s, (b) 2 rad/s, (c) 3 rad/s, and (d) 7 rad/s. (e) Amplitude ratio and (f) phase lag plots are shown for sinusoidal force tracking using frequencies ranging from 1 to 10 rad/s.

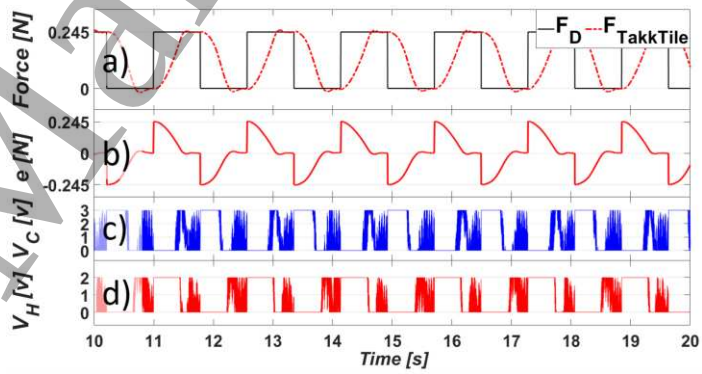

Fig. 12. (a) Force tracking of a 4 rad/s step input. (b) Force tracking error drives both the (c) cooling control voltage (4) and (d) the heating control voltage (4).

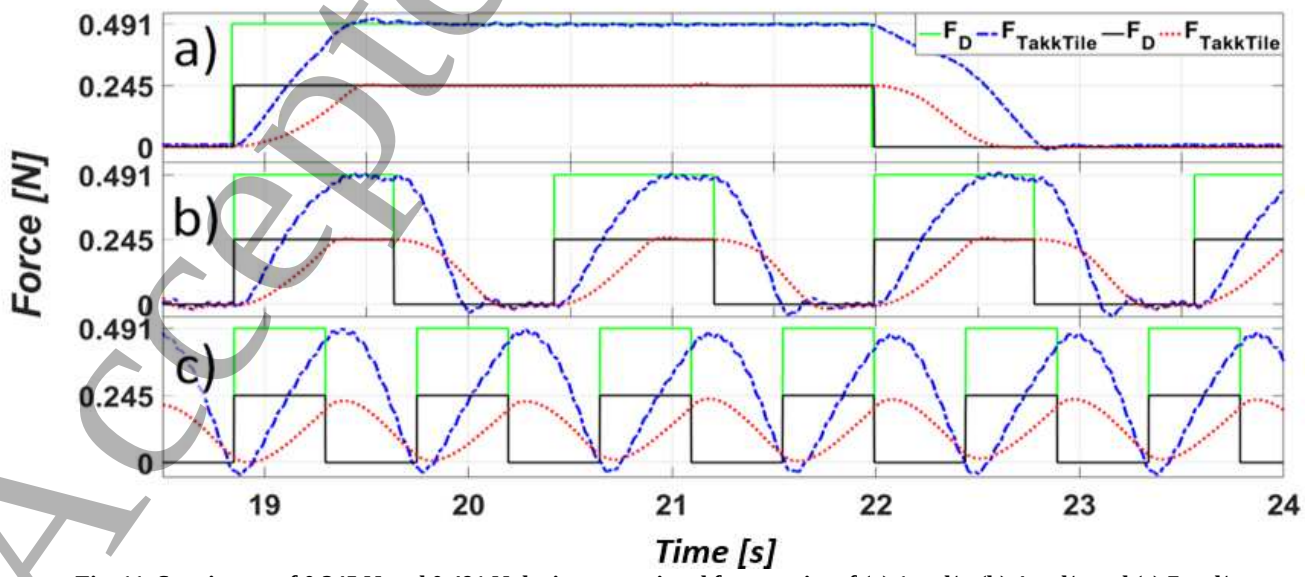

Fig. 11. Step inputs of 0.245 N and 0.491 N during operational frequencies of (a) 1 rad/s, (b) 4 rad/s and (c) 7 rad/s.

4.4 *Disturbance Rejection*

The externally applied disturbance to oppose SMA finger extension in which the cooling controller had to overcome the disturbance was compensated for with a quick response and minimal overshoot (Fig. 15(a)). The negative error during this experiment (Fig. 15(b)) caused the cooling and heating saturation functions (4) to respectively saturate at their maximum and minimum permissible levels the three times the disturbance was applied (Fig. 15(c),(d)).

In a subsequent experiment, a negative disturbance force was applied to the load cell in the negative direction to oppose flexion, where the heating controller had to overcome the disturbance (Fig. 15(e)). The resulting error was positive in this case (Fig. 15(f)) producing the opposite case of cooling and heating manifold saturation during the three instances the disturbance force was applied (Fig. 15(g),(h)). Again, the controller was able to maintain stability and rapidly recover from the externally applied disturbances.

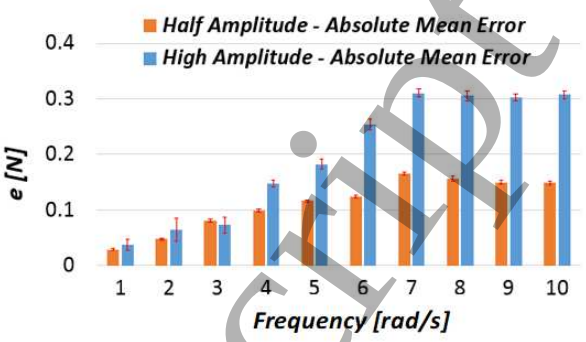

Fig. 13. Mean and standard deviation of tracking error for step inputs with half and high amplitudes of 0.245 N and 0.491 N, respectively. This was tested for frequencies ranging from 1–10 rad/s.

5. Discussion

The novel approach of using SMA tube actuators for a robotic finger has made a significant contribution in furthering the range of applications of SMA for robotic actuators. The tube form factor of the SMA actuators inherently provides an internal conduit for fluidic cooling with a compact footprint.

To rapidly cool SMA in the past, a fluid filled enclosure has been used to surround the SMA actuator, or the actuator needed to be fully submerged to provide rapid thermal cooling. The former case increases design complexity because the fluid reservoir must conform to the motion of the actuator while the latter case limits the range of applications to the underwater domain.

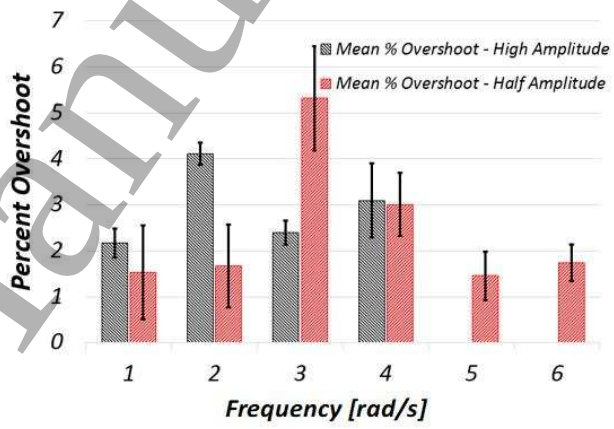

Fig. 14. Means and standard deviations of percent overshoot for high and half amplitude step inputs at frequencies ranging from 1 to 6 rad/s. There was no overshoot for higher frequencies.

In contrast, the novel MISO SMA finger presented in this paper has a bandwidth and force tracking ability comparable to the underwater finger manipulator actuated by SMA plates presented in [10], but was able to achieve this without being fully submerged in a cooling liquid. The internal conduit afforded by the SMA tubes naturally provides a channel for internal fluidic cooling that matches the motion of the actuators.

Throughout the experiments, it was observed that the Joule heating occurred more quickly than the fluidic cooling, consistent with prior observations in the field [6],[7],[9],[10],[14]. The difference in response rates during the heating and cooling portions of the actuator operation can be understood based on the different principles of heat transfer during these two different modes. Joule heating is an inherently fast process because it functions on the principle of displacing electrons through a conductive medium, in this case, the SMA tubes. In contrast to this, the cooling action in the novel finger is based on the principle of heat

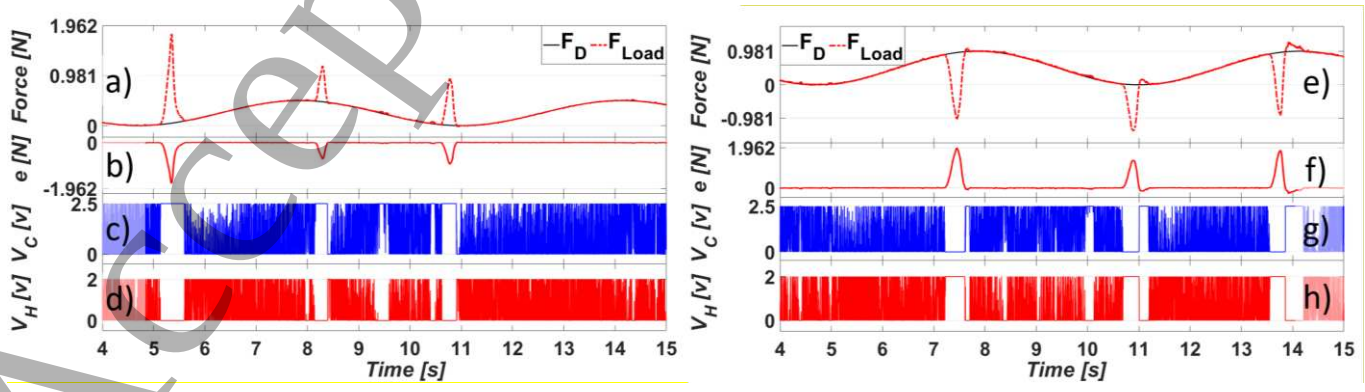

Fig. 15. (a) Force tracking, (b) error, (c) cooling and (d) heating control voltages while three disturbances were applied opposing flexion. (e) Force tracking, (f) error, (g) cooling and (h) heating control voltages while three disturbances were applied opposing extension.

convection, where heat from the SMA tubes was transferred into the cooling fluid as it was pumped through the internal conduit of the SMA actuators. The dynamics of Joule heating SMA actuators are highly nonlinear and remain an active area of research. This is because the electrical resistance of SMA changes nonlinearly during the phase transitions to and from austenite and martensite [37], which directly impacts the Joule heating effect. Similarly, the cooling rate of the SMA is highly dependent upon the thermal conductivity at the SMA-fluid interface [37], and this parameter also changes nonlinearly across the surfaces of the SMA tube actuators. Modeling efforts of SMA continues to be an ongoing area of research regarding the electrical [37], thermal [37-44], displacement [39, 40, 43, 45, 46], and force [43, 46] parameters of the numerous form factors in which SMA materials are produced [46-52]. For these reasons, a nonlinear control approach was used to guarantee robust system performance of this highly nonlinear and novel robotic finger, without significant knowledge of the system model dynamics [36].

While the application of this paper has focused on Joule heating the SMA tubes to flex the finger and increase the applied force, it is also possible that the tubes could be actuated by hot liquid pumped through the inner cavity of the tubes. This would be a valuable option in the case where electrical current would be undesirable. The tradeoff is that a valve would be required to switch between heating and cooling the SMA tubes by hot and cold liquid. It is also likely that heating the tubes with liquid would be a slower process than Joule heating, which would negatively impact the system bandwidth. However, the bandwidth of this novel robotic finger could potentially be increased by pumping very cold liquid or gas through the inner tubes to more rapidly cool them. This would need to be balanced against the ability to rapidly heat the tubes from a much colder temperature, to ascertain the optimal temperature ranges of operation.

Coupling this novel SMA tube actuation method with the external finger-like linkage mechanism provided a range of motion of the distal phalanx that is comparable to the distal phalanges of human fingers [27]. The maximum force applied by this robotic finger is comparable to those applied by fingers on commercially available prostheses such as the Vincent and Bebionic hands [33]. Additionally, this novel finger has a high strength to weight ratio: the finger has a combined mass of 30 g and can produce a fingertip force of 4.346 N. This maximum force could be further increased by optimizing the mechanical advantage of the linkage mechanism while the total mass of the finger could be reduced by a lighter material for the linkage mechanism or by machining out more aluminum from the linkage.

6. Conclusion

This paper has detailed the design and control of a novel robotic finger that is actuated by SMA tubes, which inherently enable an internal channel for fluidic cooling. This novel actuation concept has not previously been used in robotic hands, and has the potential to open new applications of SMA actuators for robotic systems without the limitation of submerging or enclosing the actuator in a cooling medium. This greatly increases the realm of operational domains for many classes of SMA actuators, and as such has great potential to positively impact the field. Force control with an integrated tactile sensor has also demonstrated the ability to precisely control the applied fingertip force and to reject external disturbances. This compact, lightweight robotic finger has low control complexity due to the antagonistically situated superelastic spring return plate, and produced a maximum force of 4.346 N. An operational bandwidth of 6 rad/s was enabled via the self-contained cooling system intrinsically afforded by the internal conduit of the SMA tube actuators.

7. Acknowledgments

This research was supported in part by NIH grant 1R01EB025819, DOE awards TOA#0000332969 and TOA#0000403076, NSF awards 1317952, 1536136, and 1659484, and by I-SENSE at FAU. The authors would like to thank Dr. Hongbo Su for assistance with the FLIR thermal imaging camera, Michael Bornstein for aid to improve the linkage mechanism, Moaed Abd for assistance with editing the paper, and Ed Henderson with design of electronics.

8. References

[1] **Y. Bar-Cohen, *High Temperature Materials and Mechanisms*. CRC Press, 2014.**

[2] **K. Otsuka and C. M. Wayman, *Shape Memory Materials*. Cambridge University Press, 1999.**

[3] **H.-T. Lee, M.-S. Kim, G.-Y. Lee, C.-S. Kim, and S.-H. Ahn, "Shape Memory Alloy (SMA)-Based Microscale Actuators with 60% Deformation Rate and 1.6 kHz Actuation Speed," *Small*, vol. 14, no. 23, p. 1801023, Jun. 2018.**

[4] **M. Sreekumar, T. Nagarajan, M. Singaperumal, M. Zoppi, and R. Molfino, "Critical review of current trends in shape memory alloy actuators for intelligent robots," Industrial Robot, vol. 34, pp. 285-294, 2007.**

[5] **A. Nespoli, S. Besseghini, S. Pittaccio, E. Villa, and S. Viscuso, "The high potential of shape memory alloys in developing miniature mechanical devices: A review on shape memory alloy mini-actuators," *Sensors and Actuators A: Physical*, vol. 158, no. 1, pp. 149–160, Mar. 2010.**

[6] **J. Mohd Jani, M. Leary, A. Subic, and M. A. Gibson, "A review of shape memory alloy research, applications and opportunities," *Materials & Design (1980-2015)*, vol. 56, pp. 1078–1113, Apr. 2014.**

[7] **Y. H. Teh and R. Featherstone, "An Architecture for Fast and Accurate Control of Shape Memory Alloy Actuators," *The International Journal of Robotics Research*, vol. 27, no. 5, pp. 595–611, May 2008.**

[8] **A. Hegana, S. I. Hariharan, and E. Engeberg, "Electromechanical Conversion of Low Temperature Waste Heat via Helical Shape Memory Alloy Actuators," IEEE/ASME Transactions on Mechatronics, 2015, DOI: http://dx.doi.org/10.1109/TMECH.2015.2481087**

[9] **S. Yan, X. Liu, F. Xu, and J. Wang, "A Gripper Actuated by a Pair of Differential SMA Springs," *Journal of Intelligent Material Systems and Structures*, vol. 18, no. 5, pp. 459–466, May 2007.**

[10] **E. D. Engeberg, S. Dilibal, M. Vatani, J.-W. Choi, and J. Lavery, "Anthropomorphic finger antagonistically actuated by SMA plates," *Bioinspir. Biomim.*, vol. 10, no. 5, p. 056002, 2015.**

[11] T. Mineta, S. Kudoh, E. Makino, T. Kawashima, and T. Shibata, "Accurate and simple assembly process of shape memory alloy tubular micro manipulator with a bias mechanism," *Microelectronic Engineering*, vol. 88, no. 8, pp. 2683–2686, Aug. 2011.

[12] Y. I. Yoo, J. W. Jeong, J. J. Lee, and C. H. Lee, "Effect of heat treatment on the two-way recovery stress of tube-shaped NiTi," *Journal of Intelligent Material Systems and Structures*, vol. 23, no. 10, pp. 1161–1168, Jul. 2012.

[13] Y. I. Yoo, J. J. Lee, C. H. Lee, and J. H. Lim, "An experimental study of the two-way shape memory effect in a NiTi tubular actuator," *Smart Mater. Struct.*, vol. 19, no. 12, p. 125002, 2010.

[14] R. Aversa *et al.*, "Biomechanically Inspired Shape Memory Effect Machines Driven by Muscle Like Acting Niti Alloys," Social Science Research Network, Rochester, NY, SSRN Scholarly Paper ID 3075373, Nov. 2016.

[15] K. Andrianesis and A. Tzes, "Development and Control of a Multifunctional Prosthetic Hand with Shape Memory Alloy Actuators," *J Intell Robot Syst*, vol. 78, no. 2, pp. 257–289, May 2015.

[16] D. Copaci, E Cano, L. Moreno, D. Blanco, New Design of a Soft Robotics Wearable Elbow Exoskeleton Based on Shape Memory Alloy Wire Actuators, Appl Bionics Biomech (2017) doi: 10.1155/2017/1605101

[17] K. J. D. Laurentis and C. Mavroidis, "Mechanical design of a shape memory alloy actuated prosthetic hand," *Technology and Health Care*, vol. 10, no. 2, pp. 91–106, Jan. 2002.

[18] K.-J. Cho and H. H. Asada, "Architecture design of a multiaxis cellular actuator array using segmented binary control of shape memory alloy," *IEEE Transactions on Robotics*, vol. 22, no. 4, pp. 831–843, Aug. 2006.

[19] A. D. Price, A. Jnifene, and H. E. Naguib, "Design and control of a shape memory alloy based dexterous robot hand," *Smart Mater. Struct.*, vol. 16, no. 4, p. 1401, 2007.

[20] J. Rosmarin and H. Asada, "Synergistic design of a humanoid hand with hybrid dc motor - sma array actuators embedded in the palm," presented at the IEEE International Conference on Robotics and Automation, Pasadena, CA, USA, 2008.

[21] V. Bundhoo, E. Haslam, B. Birch, and E. J. Park, "A shape memory alloy-based tendon-driven actuation system for biomimetic artificial fingers, part I: design and evaluation," *Robotica*, vol. 27, no. 1, pp. 131–146, Jan. 2009.

[22] A. F. C. Silva, A. J. V. dos Santos, C. da R. Souto, C. J. de Araújo, and S. A. da Silva, "Artificial Biometric Finger Driven by Shape-Memory Alloy Wires," *Artificial Organs*, vol. 37, no. 11, pp. 965–972, Nov. 2013.

[23] P. L. Bishay and A. R. Sofi, "Sensitivity analysis of a smart soft composite robotic finger design using geometrically nonlinear laminated composite finite beam elements," *Materials Today Communications*, vol. 16, pp. 111–118, Sep. 2018.

[24] F. Gao, H. Deng, and Y. Zhang, "Hybrid actuator combining shape memory alloy with DC motor for prosthetic fingers," *Sensors and Actuators A: Physical*, vol. 223, pp. 40–48, Mar. 2015.

[25] F. Simone, A. York, and S. Seelecke, "Design and fabrication of a three-finger prosthetic hand using SMA muscle wires," presented at the Proc. of SPIE; Bioinspiration, Biomimetics, and Bioreplication, 2015.

[26] E. Engeberg and S. Meek, "Adaptive sliding mode control for prosthetic hands to simultaneously prevent slip and minimize deformation of grasped objects," IEEE/ASME Transactions on Mechatronics, vol. 18, pp. 376-385, 2013, DOI: http://dx.doi.org/10.1109/TMECH.2011.2179061.

[27] J. C. Becker and N. V. Thakor, "A study of the range of motion of human fingers with application to anthropomorphic designs," *IEEE Transactions on Biomedical Engineering*, vol. 35, no. 2, pp. 110–117, Feb. 1988.

[28] M. Bergamasco, F. Salsedo, and P. Dario, "Shape memory alloy micromotors for direct-drive actuation of dexterous artificial hands," *Sensors and Actuators*, vol. 17, no. 1, pp. 115–119, May 1989.

[29] H. Rodrigue, W. Wang, D.-R. Kim, and S.-H. Ahn, "Curved shape memory alloy-based soft actuators and application to soft gripper," *Composite Structures*, vol. 176, pp. 398–406, Sep. 2017.

[30] C. Ades, S. Dilibal, and E. D. Engeberg, "Exoskeleton for tubular shape memory alloy finger with internal cooling and a superelastic SMA spring return," in *ASME Florida Conference on Recent Advances in Robotics*, 2016.

[31] Y. Tenzer, L. P. Jentoft, and R. D. Howe, "The Feel of MEMS Barometers: Inexpensive and Easily Customized Tactile Array Sensors," *IEEE Robotics Automation Magazine*, vol. 21, no. 3, pp. 89–95, Sep. 2014.

[32] D. Yoon and Y. Choi, "Underactuated Finger Mechanism Using Contractible Slider-Cranks and Stackable Four-Bar Linkages," *IEEE/ASME Transactions on Mechatronics*, vol. 22, no. 5, pp. 2046–2057, Oct. 2017.

[33] J. T. Belter, J. L. Segil, A. M. Dollar, and R. F. Weir, "Mechanical design and performance specifications of anthropomorphic prosthetic hands: A review," *The Journal of Rehabilitation Research and Development*, vol. 50, no. 5, p. 599, 2013.

[34] M. Abdeetedal and M. R. Kermani, "Grasp and Stress Analysis of an Underactuated Finger for Proprioceptive Tactile Sensing," in IEEE/ASME Transactions on Mechatronics. doi: 10.1109/TMECH.2018.2844327

[35] E. Engeberg and S. Dilibal, "Antagonistically Actuated Shape Memory Alloy Manipulator," USA Patent No. 9,744,055 B2, Aug. 29, 2017

[36] Slotine, J. J. E., & Li, W. (1991). Applied nonlinear control (Vol. 199, No. 1). Englewood Cliffs, NJ: Prentice hall.

[37] Faulkner, M. G., Amalraj, J. J., & Bhattacharyya, A. (2000). Experimental determination of thermal and electrical properties of Ni-Ti shape memory wires. Smart Materials and Structures, 9(5), 632–639. https://doi.org/10.1088/0964-1726/9/5/307

[38] Degeratu, S., Rotaru, P., Manolea, G., Manolea, H., & Rotaru, A. (2009). Thermal characteristics of Ni–Ti SMA (shape memory alloy) actuators. *Journal of thermal analysis and calorimetry*, *97*(2), 695-700.

[39] Cheng, S. S., Kim, Y., & Desai, J. P. (2017). New actuation mechanism for actively cooled SMA springs in a neurosurgical robot. *IEEE Transactions on Robotics*, *33*(4), 986-993.

[40] Tang, X., Li, K., Chen, W., Zhou, D., Liu, S., Zhao, J., & Liu, Y. (2019). Temperature self-sensing and closed-loop position control of twisted and coiled actuator. *Sensors and Actuators A: Physical*, *285*, 319-328.

[41] Nizamani, A. M., Daudpoto, J., & Nizamani, M. A. (2017). Development of faster SMA actuators. In *Shape Memory Alloys-Fundamentals and Applications*. InTech.

[42] Saunders, R. N., Boyd, J. G., Hartl, D. J., Calkins, F. T., & Lagoudas, D. C. (2018). A simplified model for high-rate actuation of shape memory alloy torque tubes using induction heating. *Journal of Intelligent Material Systems and Structures*, *29*(6), 1088-1101.

[43] Tadesse, Y., Thayer, N., & Priya, S. (2010). Tailoring the response time of shape memory alloy wires through active cooling and pre-stress. *Journal of Intelligent Material Systems and Structures*, *21*(1), 19-40.

[44] Yoo, Y. I., Jeong, J. W., Lee, J. J., & Lee, C. H. (2012). Effect of heat treatment on the two-way recovery stress of tube-shaped NiTi. *Journal of intelligent material systems and structures*, *23*(10), 1161-1168.

[45] Utter, B. (2019). Enhancing the actuation frequency of shape memory alloy wire by vibration-enhanced cooling. *Journal of Intelligent Material Systems and Structures*, *30*(20), 3177-3189.

[46] Owusu-Danquah, J. S., Saleeb, A. F., Dhakal, B., & Padula, S. A. (2015). A comparative study of Ni 49.9 Ti 50.1 and Ni 50.3 Ti 29.7 Hf 20 tube actuators. *Journal of Materials Engineering and Performance*, *24*(4), 1726-1740.

[47] Qian, S., Ling, J., Hwang, Y., Takeuchi, I., & Radermacher, R. (2015, November). Modeling and Optimization of a Novel Heat Recovery Design for Thermoelastic Cooling Systems. In *ASME 2015 International Mechanical Engineering Congress and Exposition*. American Society of Mechanical Engineers Digital Collection.

[48] Badnava, H., Kadkhodaei, M., & Mashayekhi, M. (2015). Modeling of unstable behaviors of shape memory alloys during localization and propagation of phase transformation using a gradient-enhanced model. *Journal of Intelligent Material Systems and Structures*, *26*(18), 2531-2546.

[49] **Bechle, N. J., & Kyriakides, S. (2016). Evolution of phase transformation fronts and associated thermal effects in a NiTi tube under a biaxial stress state.** ***Extreme Mechanics Letters*****,** ***8*****, 55-63.**

[50] **Xiao, Y., Zeng, P., & Lei, L. (2018). Micromechanical modeling on thermomechanical coupling of cyclically deformed superelastic NiTi shape memory alloy.** ***International Journal of Plasticity*****,** ***107*****, 164-188.**

[51] **Jiang, D., Kyriakides, S., Bechle, N. J., & Landis, C. M. (2017). Bending of pseudoelastic NiTi tubes.** ***International Journal of Solids and Structures*****,** ***124*****, 192-214.**

[52] **Jiang, D., Kyriakides, S., Landis, C. M., & Kazinakis, K. (2017). Modeling of propagation of phase transformation fronts in NiTi under uniaxial tension.** ***European Journal of Mechanics-A/Solids*****,** ***64*****, 131-142.**

[53] **Adnan, N. M. N., Ab Patar, M. N. A., Lee, H., Yamamoto, S. I., Jong-Young, L., & Mahmud, J. (2018, April). Biomechanical analysis using Kinovea for sports application. In** ***IOP Conference Series: Materials Science and Engineering*** **(Vol. 342, No. 1, p. 012097). IOP Publishing.**